Dynamic impacts on the survivability of shale gas wells piercing longwall panels

Shun Liang [a, b, c], Derek Elsworth [b], Xuehua Li [a, *], Xuehai Fu [c], Dong Yang [d], Qiangling Yao [a], Yi Wang [b]

[a] School of Mines, Key Laboratory of Deep Coal Resource Mining, Ministry of Education, China University of Mining and Technology, Xuzhou, Jiangsu 221116, China
[b] EMS Energy Institute, G3 Center and Energy and Mineral Engineering, Pennsylvania State University, University Park, PA 16802, USA
[c] School of Resources and Geosciences, China University of Mining and Technology, Xuzhou, Jiangsu 221116, China
[d] Institute of Mining Technology, Taiyuan University of Technology, Taiyuan, Shanxi 030024, China

ARTICLE INFO

ABSTRACT

Gas wells traversing active longwall panels are susceptible to failure on account of various strata movements induced by mining activities. To reveal the dynamic impacts of longwall mining on the survivability of these shale gas wells, particularly during the mining cycle as the twin flanking panels successively approach and then pass beyond the wells, a three dimensional finite element model is applied to explore the evolution of potential distress to the wells by defining the magnitudes of various well deformations. The results demonstrate that, wellbores undergo accelerated or significant deformation (increase or decrease) when each advancing panel approaches within tens of meters and the deformation stabilizes as the panel passes the well by tens (deep mining, ~300 m) or up to one hundred plus (shallow mining, ~100 m) meters. Wells are more susceptible to instability when each panel, especially the second panel, advances past the well by approximately 50 m in the case of deep mining and more than one hundred meters for shallow mining with the accumulative deformation reaching the maximum. For mining at shallow depths (~100 m), wells deform by axial compaction, longitudinal distortion, lateral compression and tension in the vicinity of the seam, and by shear in layers close to the surface. Conversely, for deep mining (~300 m) the most severe deformations are mainly restricted to the seam and its shallow roof and floor. Locating the well slightly closer to the rib of the second advancing panel (e.g., 7.5 m out from the pillar-center for a 50 m wide three-entry longwall pillar) achieves improved well integrity.

© 2015 Elsevier B.V. All rights reserved.

1. Introduction

Ensuring the stability and security of hydrocarbon wells is a crucial issue in petroleum and natural gas recovery (Aadnoy and Ong, 2003; Al-Ajmi and Zimmerman, 2006; Bradley, 1979a; Santarelli et al., 1986; Zhang et al., 1999). Deformation or instability of wellbores may have significant implications for loss of production and safety (Hale and Mody, 1993; Zeynali, 2012; Zhang et al., 2009). Long-term stability is vital for both energy development and business management. The shale gas boom has resulted from the application of modern technologies of horizontal drilling and hydraulic fracturing (Haluszczak et al., 2013) with shale reservoirs typically overlain by mineable coal seams. Such coal seams within the Appalachian Basin are mainly extracted by longwall mining, which exert significant impacts on the stability of oil and gas wells transiting these mineable coalbeds — due to the deformation of the overlying strata that occurs after the removal of individual panels (Fig. 1). Extensive field practice has indicated that, vertical gas wells in longwall mining areas mainly fail as a result of shear, distortion, compression and tension (Chen et al., 2012; Liang et al., 2014; Liu et al., 2014; Wang et al., 2013), which are principally due to the failure of rock around the borehole, occurring when stresses applied on the wellbore wall exceed the limit strength of the surrounding rock.

Generally, a protective barrier pillar is retained to protect the wellbore as it transits an unmined portion of the seam. However,

* Corresponding author.
  E-mail address: lsxh2001@126.com (X. Li).
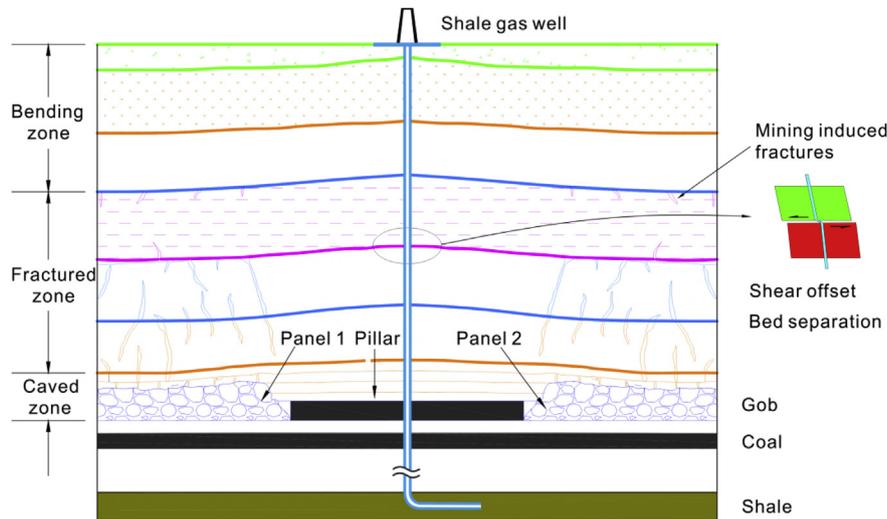
Fig. 1. Schematic diagram of a shale gas well penetrating mineable coal seams. Not to vertical scale. Three zones with different degrees of deformation form over the gob after mining (namely the Caved zone, the Fractured zone and the Bending zone). The gas well extends from the surface to the shale, penetrating a longwall pillar (modified from Singh and Kendorski, 1981).

the diameter of a gas well is usually 20—40 cm, which is far smaller than that of a vertical shaft (6—10 m) for coal mining. Therefore, gas wells are significantly more sensitive to strata movement than access shafts. Although the pillar can provide certain protection for the well, the effect of significant movements of the overlying strata induced by full extraction (longwall) mining may be damaging.

Numerous studies have explored the stability of oil and gas wells including physical—mechanical or chemical—mechanical interactions between clay minerals and drilling fluids (Hale et al., 1993; Tan et al., 1996; Zeynali, 2012). These explore the influence of mud weights, in situ stresses, rock lithology and other factors on wellbore failure (Aadnoy and Chenevert, 1987; Ajalloeian and Lashkaripour, 2000; Bradley, 1979b; Gough and Bell, 1981; Haimson and Song, 1993; Lee et al., 2012; Niandou et al., 1997; Ong and Roegiers, 1993; Santarelli et al., 1986; Tan et al., 1998; Tan and Willoughby, 1993; Tien et al., 2006). However, fewer investigations have probed the effects of mining-induced deformations. This is particularly relevant in areas such as southwest Pennsylvania, West Virginia, and eastern Ohio, in the United States where active longwall mining recovers seams that overlay the gas reservoirs. Boreholes to extract hydrocarbons penetrate these shallow minable coal seams before reaching the target shale gas horizons. However, the effect of longwall mining on the stability of such wells has not been highlighted until recently (Liang et al., 2014; Rostami et al., 2012; Scovazzo and Russell, 2013; Wang et al., 2013). This issue of instability of gas wells in longwall mining areas has only recently come to the fore since the rapid development of shale gas. Nonetheless, an update is necessary because gas and oil well construction and coal mining have changed considerably since the original requirements for such wells were enacted in 1956. These changes to common practice include well diameter, casing and pipe steel, cementing requirements, mine configurations, seam depths, and extraction thicknesses (Scovazzo and Russell, 2013).

The survivability of gas wells can be informed by parallel studies probing the performance of gob gas ventholes (Karacan, 2009a,b; Karacan and Goodman, 2009; Karacan and Olea, 2013; Whittles et al., 2006, 2007), the three dimensional influence of coal mining on ground-water supplies (Elsworth and Liu, 1995; Liu and Elsworth, 1997, 1999) and on the stability of gate roads underground (Shabanimashcool and Li, 2012). In particular, the

relationship between changing reservoir conditions, longwall face position, and surface movement is likely important (Schatzel et al., 2012).

In this work, we extend a two-dimensional modeling study on the stability of gas wells in longwall mining areas (Liang et al., 2014) to explore whether the peak strains are indeed reached in the two-dimensional section or whether these are merely muted relative to the true 3D strains induced around the true 3D mining geometry. This study addresses this issue.

2. Mechanistic model

In this work, a large scale three dimensional model is used to replicate the morphology of interbedded shales and sandstones or limestones adjacent to a coal seam and with the deformability properties of the units and interfaces controlling the response. We examine the distribution and dynamic evolution of shear offsets, bed separation and compression and various strains along vertical well trajectories induced by mining activities, as the twin flanking panels successively approach and pass by these wells. Finally, we evaluate the three dimensional impacts of longwall mining upon the performance and stability of wells.

2.1. Strata/well deformation

Modes of borehole instability for gas wells transiting coalbeds extracted by longwall mining can be classified into several categories: *first*, shear failure due to the dissimilarity of rock properties and incongruity of horizontal movement (shear offset) and longitudinal distortion between adjacent layers; *second*, tensile failure resulting from the incompatibility in vertical displacements (bed separation) between adjacent layers; *third*, compressional failure resulting from concentrated compressive stresses both in the vertical (penetration/compression occurs within the seam and at weak interfaces between layers, especially at interfaces between the seam and its immediate roof and floor) and horizontal (extrusion/squeeze occurs in the vicinity of the seam) directions; and *fourth*, combining forms of shear and tension or shear and compression. Among these modes, gas wells are most susceptible to fail by shear and distortion, which has been indicated in practice (Chen et al., 2012; Liang et al., 2014; Liu et al., 2014; Rostami et al., 2012;

Wang et al., 2013). Typical deformations of a well within and between layers of alternating soft shale and stiff sandstone as the well is sheared, distorted, stretched and compressed by strata movement induced by coal mining are illustrated in Fig. 2. In this figure, Δd is the relative vertical motion between the upper and lower beds ($\Delta d > 0$ corresponds to bed separation and $\Delta d < 0$ is for bed penetration/compression) and F, T and τ are respectively the compressive stress, tensile stress and shear stress imposed on the well casing. Magnitudes of well deformation can be calculated from the following expressions.

$$U_{\text{off}-\text{H}} = \sqrt{U_{\text{off}-\text{x}}^2 + U_{\text{off}-\text{y}}^2} \tag{1}$$

$$U_{\text{off}-\text{x/y}} = U_{(i,j+1)-\text{x/y}} - U_{(i,j)-\text{x/y}} \tag{2}$$

$$\gamma_{\text{max}} = \sqrt{\gamma_{\text{xz}}^2 + \gamma_{\text{yz}}^2} \tag{3}$$

where, $U_{\text{off-H}}$, $U_{\text{off-x}}$ and $U_{\text{off-y}}$ are respectively the total horizontal shear offset on the X-Y plane (horizontal plane) and its two components — the lateral shear offsets in the X and Y directions (Table 1). $U_{(i,j)-\text{x/y}}$ and $U_{(i,j+1)-\text{x/y}}$ are the horizontal displacements of two adjacent nodes at one interface in the X/Y direction. γ_{xz}, γ_{yz} and γ_{max} are respectively shear strains in the X-Z plane, Y-Z plane and the total longitudinal distortion of the vertical well (Table 1). We utilize these relations to calculate the deformations that a well would undergo with the movement of the overlying and underlying strata resulting from longwall mining.

2.2. Failure criterion and formulation

In this analysis we neglect any added resistance applied by well casing — as this resistance will be trivial in comparison to the applied deformations. Consequently, we do not mesh the well, but use quantities (displacements and strains) of a series of nodes and zones which correspond to the five candidate vertical well trajectories to demonstrate the specific characteristics of wellbore deformation.

Shear is the primary mode of wellbore instability for gas wells penetrating alternating soft and stiff beds under the effects of longwall mining. We adopt the Mohr—Coulomb strength criterion to determine whether the surrounding rock will yield, with this criterion is defined as

$$\tau_f = c + \sigma_{\text{n}} \tan\phi \tag{4}$$

where, τ_f is the shear strength, c is the cohesion, σ_{n} is the normal stress and ϕ is the angle of internal friction. This can also be expressed in the form

$$\sigma_1 = \frac{1 + \sin\phi}{1 - \sin\phi}\sigma_3 + \frac{2c\,\cos\phi}{1 - \sin\phi} \tag{5}$$

where, σ_1 and σ_3 are respectively the maximum and minimum principal stresses.

2.3. Interface characteristics

Within the Appalachian Basin in western Pennsylvania, the Pittsburgh coal seam is the most economically important coalbed, of which the overlying and underlying strata mainly comprise soft shales interbedded with stiff sandstone or limestone. The most common failure mode for gas wells piercing longwall panels is by shear instability, which occurs at weak interfaces between the layered strata. In order to fully replicate the probable response of weak interfaces between layers, interface elements are adopted in our model to represent the weak contact along which slippage, bed separation and compression may occur.

We use the model FLAC3D (Itasca, 2009) with interfaces characterized by Coulomb sliding and tensile and shear bonding. Each interface element is defined by three interface nodes. Generally, interface elements are attached to a surface face. When another grid surface comes into contact with an interface element, the contact is detected at the interface node, and is characterized by normal and shear stiffnesses, and strength. The fundamental contact relation is defined between the interface node and a face (the target face). The constitutive model of the interface element is defined by a linear Coulomb shear-strength criterion which limits
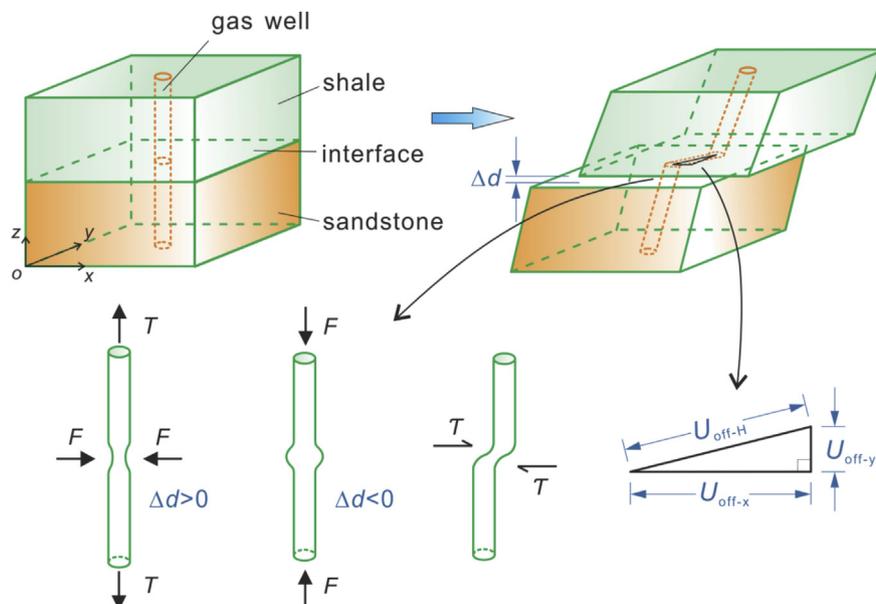

Fig. 2. Typical deformation of a well within and between layers of alternating soft shale and stiff sandstone as the well is sheared, distorted, stretched and compressed by strata movement induced by coal mining (with slip interfaces between alternating layers) (modified from Liu et al., 2014).

Table 1
Nomenclature for various physical quantities (deformations) discussed in the following and related details.

Quantity	Description		Direction	Unit
$U_{\text{off-H}}$	Relative horizontal motion between	Total horizontal shear offset	Along the horizontal plane (X-Y) (Fig. 6)	mm
$U_{\text{off-x}}$	adjacent nodes along a well trajectory	One component of $U_{\text{off-H}}$	Along the X axis (the transverse direction)	
$U_{\text{off-y}}$		One component of $U_{\text{off-H}}$	Along the Y axis (the mining direction)	
Δd	Relative vertical motion between	Bed separation, $\Delta d > 0$	Along the Z axis (the longitudinal direction)	
	adjacent layers	Bed compression, $\Delta d < 0$		
γ_{max}	Shear strain	Total longitudinal well distortion	In 3D space (X-Y-Z)	Dimensionless, millistrain (10^{-3})
γ_{xz}		One component of γ_{max}	On 2D plane (X-Z)	
γ_{yz}		One component of γ_{max}	On 2D plane (Y-Z)	
ε_{xx}	Horizontal strain		Along the X axis (the transverse direction)	
ε_{yy}			Along the Y axis (the mining direction)	
ε_{zz}	Vertical strain		Along the Z axis (the longitudinal direction)	

the shear force acting at an interface node, the normal and shear stiffnesses (k_n and k_s), the tensile and shear bond strengths (σ_t and S_s), and the dilation angle (ψ) that causes an increase in effective normal force on the target face after the shear-strength limit is reached (Itasca, 2009). Fig. 3 illustrates the components of the constitutive model acting at the interface node — P. The relationship between shear stress and shear displacement is illustrated in Fig. 4 where the curve includes two parts: the linear elastic stage and the perfectly plastic stage.

In the linear elastic regime (Fig. 4), the normal and shear forces that describe the elastic interface response at calculation time ($t+\Delta t$) are determined by Eq. (6):

$$F_n^{(t+\Delta t)} = k_n u_n A + \sigma_n A$$
$$F_{si}^{(t+\Delta t)} = F_{si}^{(t)} + k_s \Delta u_{si}^{(t+(1/2)\Delta t)} A + \sigma_{si} A \qquad (6)$$

where, $F_n^{(t+\Delta t)}$ and $F_{si}^{(t+\Delta t)}$ are separately the normal force and the shear force vector at time ($t + \Delta t$); u_n is the absolute normal penetration of the interface node into the target face; Δu_{si} is the incremental relative shear displacement vector; σ_n is the additional normal stress added due to interface stress initialization; k_n is the normal stiffness; k_s is the shear stiffness; σ_{si} is the additional shear stress vector due to stress initialization at the interface; and A is the representative area associated with the interface node.

In the perfectly plastic regime (Fig. 4), the contact states of the interface node can be divided into three types according to the Mohr–Coulomb criteria: (1) the slip while in a bonded state, (2) the Coulomb sliding state, and (3) the separated state. The yield relationships in the shear and normal directions are

$$F_{\text{smax}} = cA + \tan\phi(F_n - pA)$$
$$F_n = \sigma_t \qquad (7)$$

where F_{smax} is the maximum shear strength, c is the cohesion along the interface, ϕ is the friction angle of the interface, F_n is the normal force, p is the pore pressure, and σ_t is the normal tensile strength of the interface.

At every calculation time t, the normal force F_n and shear force F_{si} of the interface nodes are compared with the normal tensile strength σ_t and the maximum shear strength F_{smax}, respectively. If the interface force exceeds the interface strength, the force will be corrected as follows (Itasca, 2009):

(1) If $F_n < \sigma_t$ and $F_{si} < F_{\text{smax}}$, then the interface node remains in the elastic regime, failing to slip while bonded. The interface forces are not corrected.
(2) If $F_n < \sigma_t$ and $F_{si} \geq F_{\text{smax}}$, then the interface node falls in the Coulomb sliding regime and the interface forces are corrected. Since we neglect the dilation characteristics of the interface elements, the forces are corrected as follows:

$$F_{si} = F_{\text{smax}} \qquad (8)$$

(3) If $F_n \geq \sigma_t$, then the interface node falls into the separation regime, and the interface forces are corrected as follows:

$$F_n = 0$$
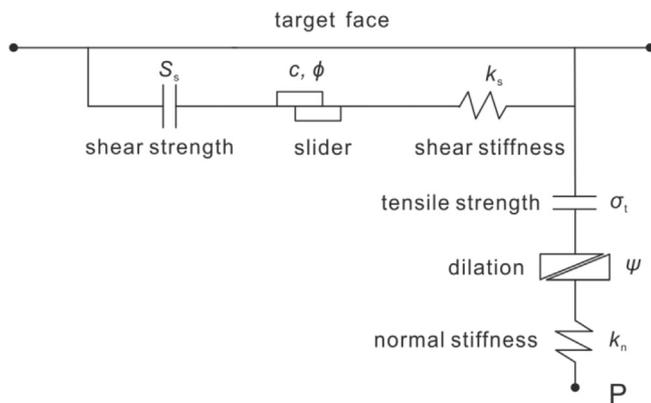$$F_{si} = 0 \qquad (9)$$
$$\sigma_t = 0$$

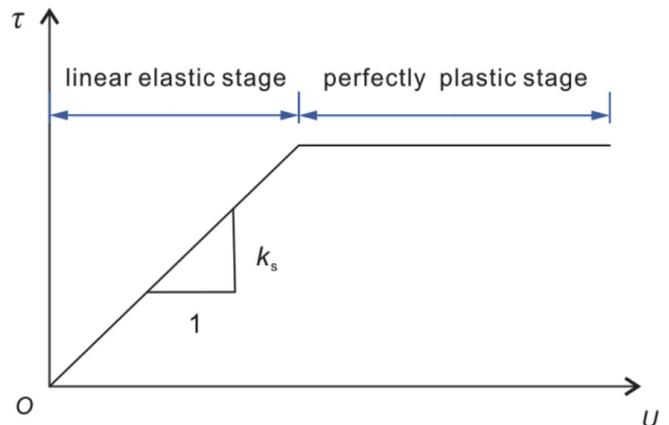**Fig. 3.** Components of the bonded interface constitutive model (Itasca, 2009).

Fig. 4. Relationship between shear stress τ and shear displacement U of interface element (Wu et al., 2011).

3. 3D geomechanical model

A large scale three-dimensional geomechanical model is constructed using the commercial software code FLAC3D (Itasca, 2009). This is an explicit finite-difference program for engineering mechanics with a wide range of constitutive models available to simulate the behavior of rock and soils. It has been widely applied to the modeling of longwall workings in coal measure strata (Mohammad et al., 1997; Whittles et al., 2007; Yavuz and Fowell, 2002).

3.1. Geological condition and parameters

The Pittsburgh coal seam and its overlying and underlying strata within the Appalachian Basin mainly comprise layered strong sandstones or limestones and relatively weak shales. We simplify this model to one comprising a single 2 m thick coalbed with alternating massive shale and sandstone layers each ~10 m thick (Fig. 5). We employ the same rock property parameters in the 3D model as used in a previous 2D study (Liang et al., 2014), which was calibrated against observed and recorded surface subsidence in the Appalachian coalfields (Gutierrez et al., 2010).

3.2. Model geometry and settings

The entire model is 600 m long × 2000 m wide × 142/342 m thick with a flat ground surface. Panels 1 and 2, which have the same dimension (600 m long × 370 m wide × 2 m thick), straddle a 50 m wide central pillar that incorporates a 15 m wide yield pillar, a 5 m wide gate road and a 30 m wide barrier pillar, as illustrated in Figs. 5 and 6. The X, Y, Z axes comprise the panel rib (Y), the transverse direction (X) with the Z axis along the vertical well axis. Extra elements (605 m wide) are added to ensure that the edges of the model along the X axis are undisturbed by stress or strain induced by excavation. The lateral boundaries along the X and Y axes are fixed for normal displacements. The basal boundary is fixed in the vertical direction and the upper boundary is stress-free.

The model is run to an initial equilibrium by gravity loading to assign the pre-mining stress condition. Then the gate road, followed by panel 1 and then by panel 2 are excavated sequentially. Panel advance is simulated by stepwise excavation — using twenty-eight stages for each panel. Locations of the panels after each excavation stage are indicated in Fig. 6, for the five candidate well trajectories all located at the Y coordinate of 300 m. Each panel advances 10 m in each excavation stage as it approaches and then passes-by the well within a distance of ±100 m in the direction of the Y axis but advances by a greater increment (100 m, 50 m, 30 m and 20 m, sequentially) when the panel is more than 100 m ahead of these wells or when the panel is more than 100 m beyond these wells (20 m, 30 m, 50 m and 100 m, sequentially) (Fig. 6).

We observe that both the cases of a shallow seam (~100 m) and a deeper seam (~300 m) result in larger deformation for gas wells compared to the case of a seam at intermediate depth ~200 m (Liang et al., 2014). Correspondingly, in this work we explore these two bounding scenarios. We examine the potential performance of five typical well trajectories under the dynamic effects of longwall mining as illustrated in Figs. 5 and 6.

4. Analysis and discussion of model results

We examine the deformation of the overlying layered strata as it is undermined, stretched, tilted, then lowered, and finally recompacted (McNally and Evans, 2007). The overlying beds deform in both vertical and horizontal directions, such that a slow-moving subsidence profile forms across the ground surface (Peng, 1992;

Peng and Chiang, 1984). Consequently, mining stresses/strains are induced within the coal seam and its overburden and underburden, especially at panel corners where the mining induced stresses in front of the working face (the front abutment pressure) and along both sides of the gob (the side abutment pressure) superimpose (Fig. 7) (Peng, 1986), and within which wells may be located. Hence, the loading process due to mining-induced stresses on these vertical wells penetrating the pillar is not static but dynamic and changes as the flanking panels proceed in succession. These resulting large strains exert significant deformations on wells, leading to progressive deformation and potentially failure.

We explore this deformation behavior in this analysis. With recovered data of deformations, strains and distortions we evaluate the potential performance of wells under the dynamic impacts of longwall mining to define the potential for failure through the full mining cycle. For clarity, deformations and strains discussed in the following are detailed in Table 1.

4.1. Evolution and magnitudes of horizontal shear offsets

We compare the total horizontal shear offset (U_{off-H}) and its two components (U_{off-x} and U_{off-y}) occurring at weak interfaces between alternating monolithic shales and sandstones, for wells penetrating both shallow (100 m) and deep (300 m) seams. The two components of shear offsets are separately in the direction perpendicular to (U_{off-x}) and parallel to (U_{off-y}) that of panel advance (Fig. 6). Profiles of U_{off-H}s and the two components for the five well trajectories passing through the pillar in the two scenarios are shown in Figs. 8–11. Fig. 8 displays the evolution of the largest U_{off-H} of each trajectory along its axis as the twin flanking panels proceed sequentially. Figs. 10 and 11 are for the two components, in which we do not show the negative U_{off-x}s and U_{off-y}s for wells piercing the shallow seam (100 m), because they are insignificant in comparison to the positive displacements. Fig. 9 illustrates the axial distribution of U_{off-H}s as each panel advances far enough beyond these wells which penetrate both shallow and deep seams. The magnitudes of U_{off-H} and its two components for each scenario are listed in Table 2.

4.1.1. Total horizontal shear offsets — U_{off-H}

As apparent in Fig. 8, for wells penetrating both the shallow (100 m) and the deep (300 m) seams, evolution of the largest U_{off-H}s along each well axis in the mining cycles of the twin panels displays similar staged characteristics. All the largest U_{off-H}s increase as panel 1 approaches and then passes these wells, but it depends on different wells in the mining cycle of panel 2. When mining the shallow seam (100 m), development of the largest U_{off-H}s may be separated into three stages according to the evolution characteristic as panel 1 proceeds. The greatest U_{off-H}s increase slowly until the working face is ~70 m ahead of the well (Stage I, <−70 m), U_{off-H}s grows no more than 4 mm as panel 1 proceeds each 10 m. Then in Stage II (−70 m to 120 m), the largest U_{off-H}s of wells increase rapidly and the peak growth could be ~10 mm for a face advance of 10 m. The peak growth is for path 1 as panel 1 advances 30–40 m after the well. In Stage III (>120 m), U_{off-H}s increase gradually again, entering a steady-state with a peak U_{off-H} of 144 mm (path 1). In the excavation cycle of panel 2, the largest U_{off-H}s of wells also build rapidly as panel 2 advances ~50 m ahead of and up to ~120 m after these wells have been passed (Stage II). The greatest U_{off-H}s of wells 1–3 decrease rapidly, however, the peak U_{off-H}s for wells 5 and 4, which are closer to panel 2, switch to increase successively under the increasing influence of mining of panel 2 as it proceeds. The peak growth is ~7 mm with an advance of 10 m, and is for path 5 as panel 2 advances 30–40 m after the well. All the U_{off-H}s remain constant as panel 2 proceeds sufficiently far (Stage III, >120 m) after wells.

As for wells penetrating the deep seam (300 m), development of
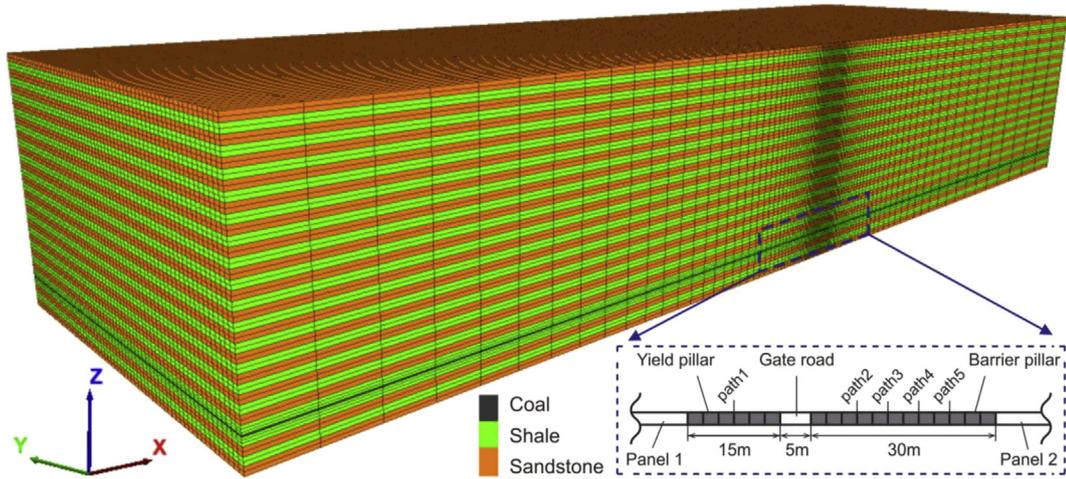
Fig. 5. A snapshot of the geometry of the large scale 3D geological model, with a 2-m thick coal seam at a depth of 100/300 m below the ground surface and with twin panels flanking a central pillar. Panel 1 (left) advances first and panel 2 (right) afterwards. Trajectories for wells 1–5 passing through both the yield and barrier pillars are located, respectively, at a lateral distance of 7.5 m from the left edge of the yield pillar (well 1), 7.5 m from the intervening gate road (well 2) and 17.5 m, 12.5 m and 7.5 m to the right edge of the barrier pillar (wells 3–5).
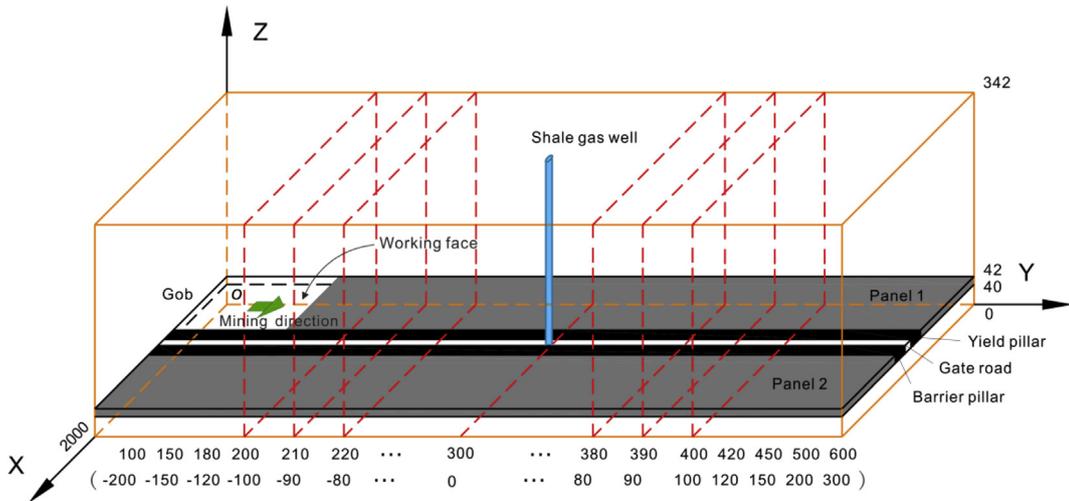

Fig. 6. The progressive excavation of each panel in the large scale three-dimensional model. Numbers in parenthesis represent the relative distance of wells from the working face after each stage of excavation. Negative magnitudes indicate that the advancing face is ahead of the well and positive magnitudes indicate that the face has passed the well.
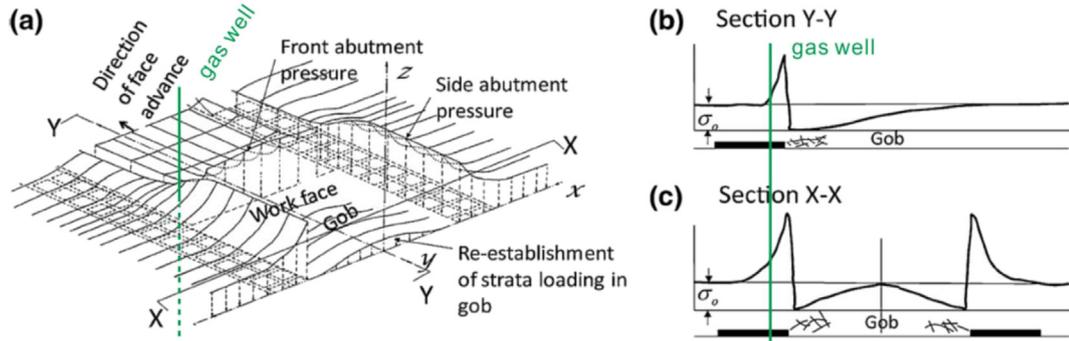

Fig. 7. Schematic of abutment stress distribution around a longwall panel (modified from Luo, 1997). σ_0 refers to the virgin (pre-mining) overburden stress.

the greatest $U_{\text{off-H}}$s displays similar characteristic to that for wells penetrating the shallow seam as panels 1 and 2 proceed successively. Shear slippage builds as panel 1 approaches within 50 m of

the well and advances less than 50 m beyond these wells (Stage II, −50 m to 50 m); the peak growth of $U_{\text{off-H}}$s is 18 mm, and is for path 1 as panel 1 advances 0–10 m after the well. In the mining
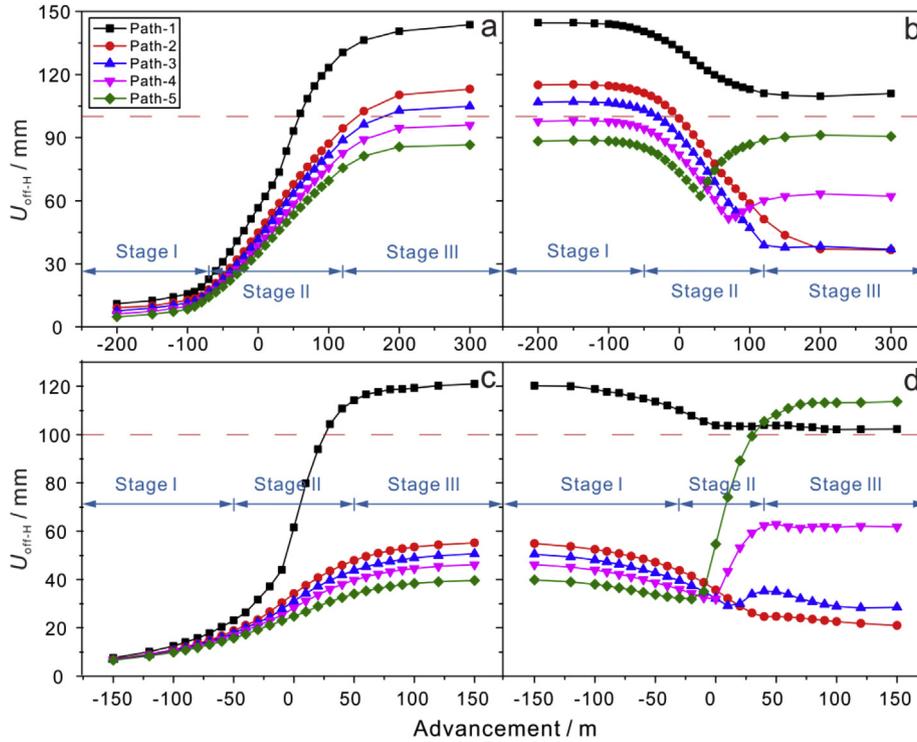
Fig. 8. Dynamic evolution of the largest total horizontal shear offsets (U_{off-H}s) along well axes occurring at weak interfaces for the five candidate paths of wells piercing both the shallow (100 m) (a, b) and the deep (300 m) (c, d) seams. Panel 1 is extracted first (a, c) and then panel 2 (b, d). The abscissa represents the relative distance (m) between wells and panels. The negative coordinates correspond to locations of the longwall working face ahead of wells which are located at an abscissa of zero, with positive magnitudes corresponding to locations of the working face as it passes-by these wells.
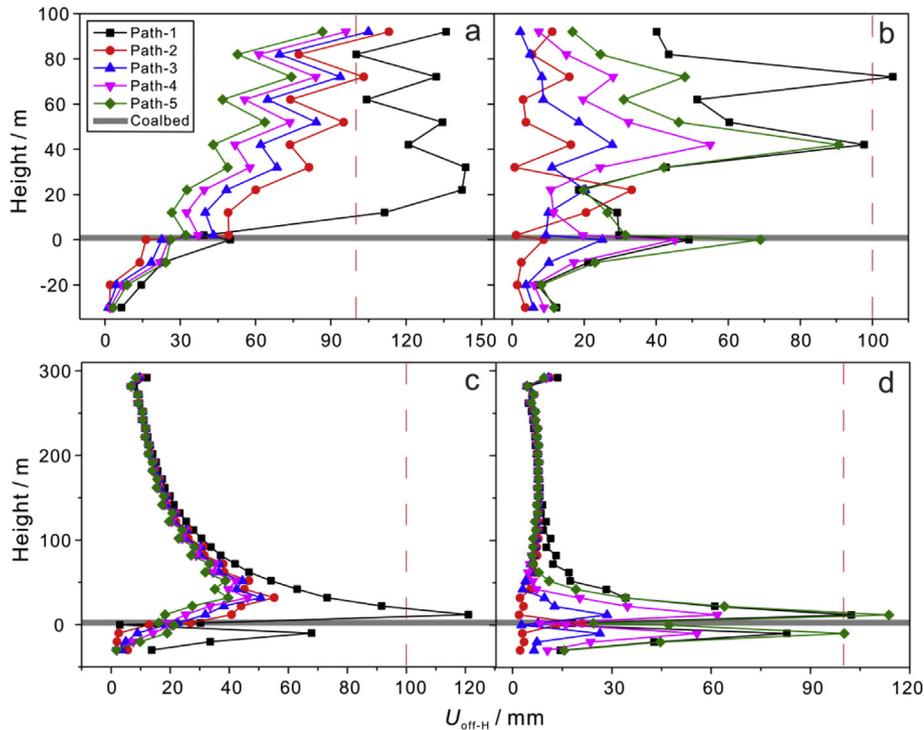
Fig. 9. Longitudinal distribution of the total horizontal shear offsets (U_{off-H}s) occurring at weak interfaces for the five candidate paths of wells after the single panel 1 (a, c) and then panel 2 (b, d) separately advance sufficiently far (300 m for wells piercing the 100 m deep seam (a, b) and 150 m for wells piercing the 300 m deep seam (c, d)) after these wells.
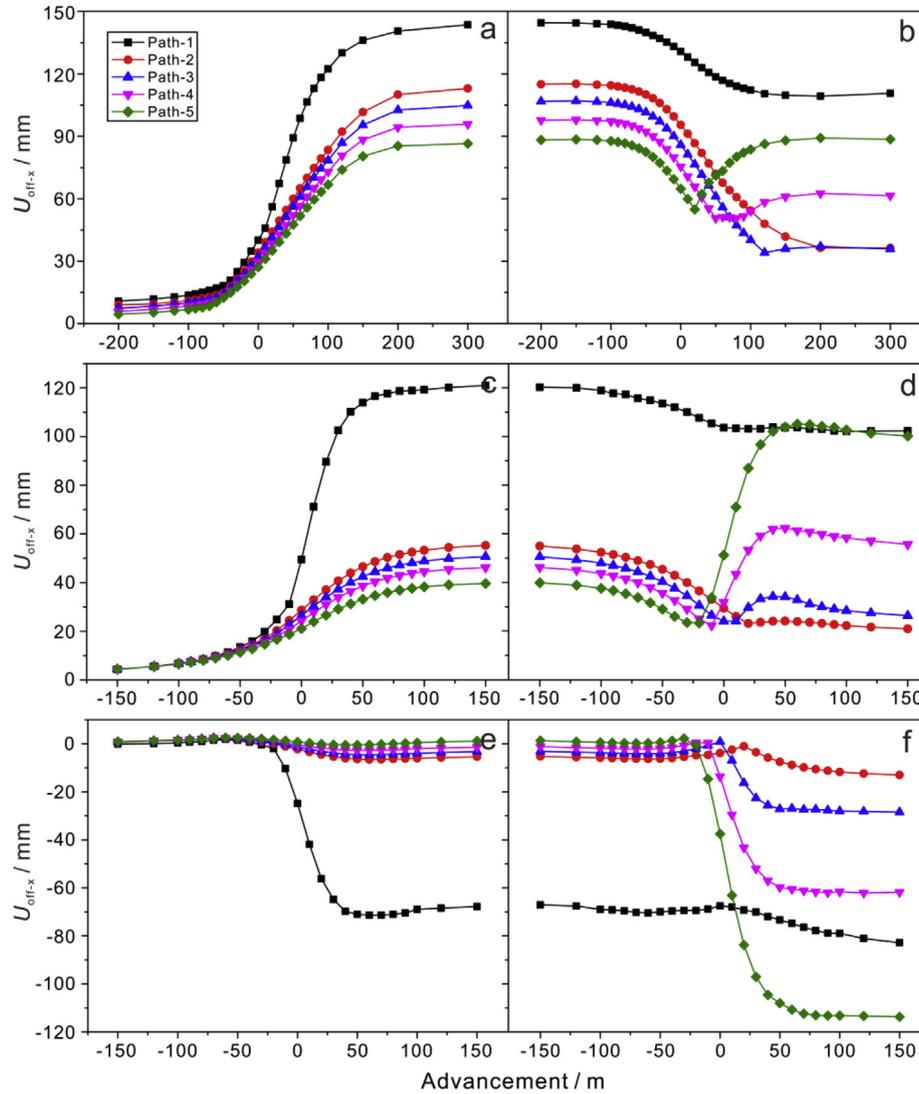
Fig. 10. Dynamic evolution of the largest (both positive and negative) lateral shear offsets − U_{off-x}s (the component along the direction parallel to the face) along well axes occurring at weak interfaces for the five candidate paths of wells, which penetrate both the shallow (100 m, a, b) and deep seams (300 m, c−f), as the twin flanking panels sequentially advance. Panel 1 is first extracted (a, c, e), followed by panel 2 (b, d, f).

cycle of panel 2, U_{off-H}s changes rapidly as panel 2 advances within 30 m ahead of and less than 40 m after these wells (Stage II, −30 m to 40 m). Thereafter, U_{off-H}s of wells 1 and 2 decrease continually, but U_{off-H}s of wells 5, 4 and 3, which are closer to panel 2, switch to increase successively under the growing mining influence of panel 2. The peak growth is 20 mm with an advance of 10 m and for path 5 as panel 2 proceeds 0−10 m after the well. All the U_{off-H}s tend to be invariant after panel 2 passes these wells by ~60 m.

Clearly in this cycle, shear deformations on wells undergo a repeated cyclic loading as the flanking twin panels successively approach and pass. Shear deformation is maximum when the face approaches within tens of meters and remains for more than one hundred meters after the panels have passed beyond these wells. The specific range where the strong influence of mining endures varies with seam depth and the relative distance between well trajectories and the twin panels. Generally, along the mining direction, the range of strong influence of mining on shear slippage across wells is broader for shallow-mining than for the case of a deeper seam.

Along the longitudinal direction, when mining is shallow

(100 m), the largest U_{off-H} (144 mm) arises in the shallow roof (20/30 m above the seam) for candidate path 1, but elevates to interfaces close to the ground surface (90 m) for paths 2−5 after panel 1 is extracted. Then these U_{off-H}s migrate to interfaces at an elevation around the half depth of the seam, and the peak U_{off-H} changes to be 111 mm. When mining is deep (300 m), U_{off-H}s of wells all peak on weak interfaces within the shallow roof (10−30 m) either after panel 1 (121 mm) is, or both panels (114 mm) are extracted. The U_{off-H}s on interfaces within shallower layers are much smaller. U_{off-H}s occur on weak interfaces more than 60 m above the seam are all less than 15 mm when the twin panels are both mined (Fig. 9d). Referring to these longitudinal distributions of U_{off-H}s, the length of protective casing or grouting of the surrounding rock can be designed. Besides, along the well axis, U_{off-H} fluctuates as the strength of overlying beds varies. The U_{off-H} on one weak interface with a stiffer layer above and a soft layer below is generally larger than as occurs on the interface with a softer layer above and a stiffer one below, which is even more apparent when mining is shallow.

In this study, we still define the threshold for well instability by
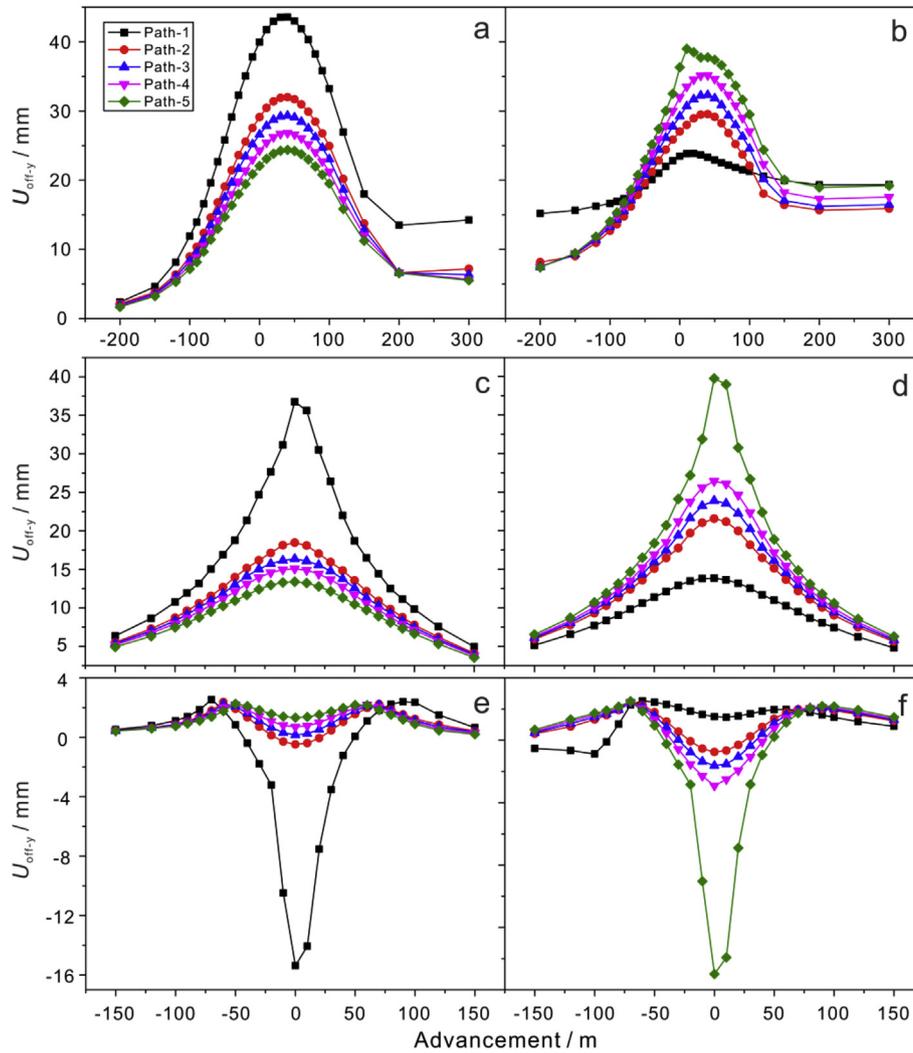
Fig. 11. Dynamic evolution of the largest (both positive and negative) lateral shear offsets – U_{off-y}s (the component along the mining direction) along well axes occurring at weak interfaces for the five candidate paths of wells, which penetrate both the shallow (100 m, a, b) and deep seams (300 m, c−f), as the twin flanking panels advance sequentially. Panel 1 is first extracted (a, c, e), followed by panel 2 (b, d, f).

shear as 100 mm (Liang et al., 2014), which corresponds to the maximum allowable horizontal shear offset, as indicated by the dashed lines in Figs. 8 and 9. For shallow mining (100 m) (Fig. 8a, b), path 1 shears first as panel 1 advances ~60 m after the well, and the

accumulated U_{off-H}s of paths 2 and 3 exceed the threshold as panel 1 advances 150 and 200 m separately after the wells. Only the remainder U_{off-H} of path 1 is still greater than 100 mm as panel 2 is sufficiently extracted (>120 m). For deep mining (300 m) (Fig. 8c,

Table 2
Statistical results of relative motion occurring on weak interfaces between adjacent layers both in the horizontal and vertical directions (horizontal shear offsets, bed separation and compression) for wells piercing a seam at a depth of 100 m and 300 m in the mining cycle of panels 1 and 2.

Seam depth	Relative motion between adjacent layers/mm		Panel 1	Hazardous locations/m		Panels 1 and 2	Hazardous locations/m		Percentage change
				Height	Advancement		Height	Advancement	
100 m	U_{off-H}		144	+30/+90	>200	111	+40	>150	−23%
	U_{off-x}		−31 to 144	–	–	−89 to 111	–	–	187%/−23%
	U_{off-y}		−3 to 44	–	–	−9 to 39	–	–	–
	Δd	>0	2	+90	–	0.4	+90	–	−70%
		<0	−209	±0	>120	−274	±0	>120	31%
300 m	U_{off-H}		121	+10	>60	114	+10	>50	−6%
	U_{off-x}		−71 to 121	–	–	−114 to 105	–	–	61%/−13%
	U_{off-y}		−15 to 37	–	–	−15 to 40	–	–	–
	Δd	>0	23	+30	+50	9	+110	+100	−61%
		<0	−279	±0	>50	−341	±0	>50	22%

Note: Hazardous height refers to an elevation (m) above (positive) or below (negative) the coal seam where shear offset reaches the peak and the well is most likely to fail by shear; and heights "±0" refer to the interfaces between the seam and its immediately roof and floor.

d), U_{off-H} of path 1 reaches the threshold as panel 1 advances ~30 m after the well and it is ~40 m for path 5 as panel 2 passes-by the well. U_{off-H}s of paths 2−4 are always less than 100 mm in the entire mining cycle of the twin panels. Thus, wells piercing a 100 m deep seam are more susceptible to shear than those piercing a 300 m deep seam. The unfavorable influence resulting from the mining of panel 2 is more severe for paths 5 and 4 across the pillar and is mainly manifest in the vicinity of the seam (Fig. 8b, d and Fig. 9b, d).

From the foregoing analyses, it is apparent that the rock movement and deformation within the thinner overlying strata of a shallow seam (100 m) are more severe, and the range of strong influence induced by shallow mining is relatively broad along both the transverse and mining directions. While for deep mining, strata movement (and associated deformation of wells) is mainly restricted to the shallow roof, and engenders a smaller influence along the mining direction. In the cross-section of the pillar, it is advisable to locate the well slightly closer to the second advancing panel (e.g., along candidate path 3, which is 7.5 m from the pillar center on the side of panel 2) irrespective of seam depth in order to minimize shear slippage during the entire mining cycle of panels 1 and 2.

4.1.2. Shear offsets − U_{off-x} and U_{off-y}

Figs. 10 and 11 show the evolution of the two components (U_{off-x} and U_{off-y}) of the total horizontal shear offset (U_{off-H}) along the well axis for wells penetrating both shallow and deep seams as the twin flanking panels advance sequentially, where the small negative U_{off-x}s and U_{off-y}s for wells piercing the shallow seam (100 m) are not presented (they are much smaller than the positive magnitudes). As apparent in Fig. 10, evolution of the component $−U_{off-x}$ as the twin panels advance sequentially displays similar characteristics and magnitudes to that of U_{off-H}, (Table 2). In terms of the contribution to the U_{off-H} between U_{off-x} and U_{off-y}, the former contributes the largest. Nevertheless, development of the component $−U_{off-y}$ shows a different feature. U_{off-y}s are considerably smaller in magnitude (the peak U_{off-y} is approximately one third of the peak U_{off-x}), whose evolution is approximately symmetrical as each panel advances. The symmetry plane lags behind the wells by ~35 m for shallow mining and abreast of the wells for deep mining. U_{off-y}s increase slightly first, then grow rapidly to a peak before declining rapidly to a residual displacement (Fig. 11). Along the transverse direction, both the positive and negative U_{off-y}s are greatest for path 1 (~40 mm) in the mining cycle of panel 1 and for
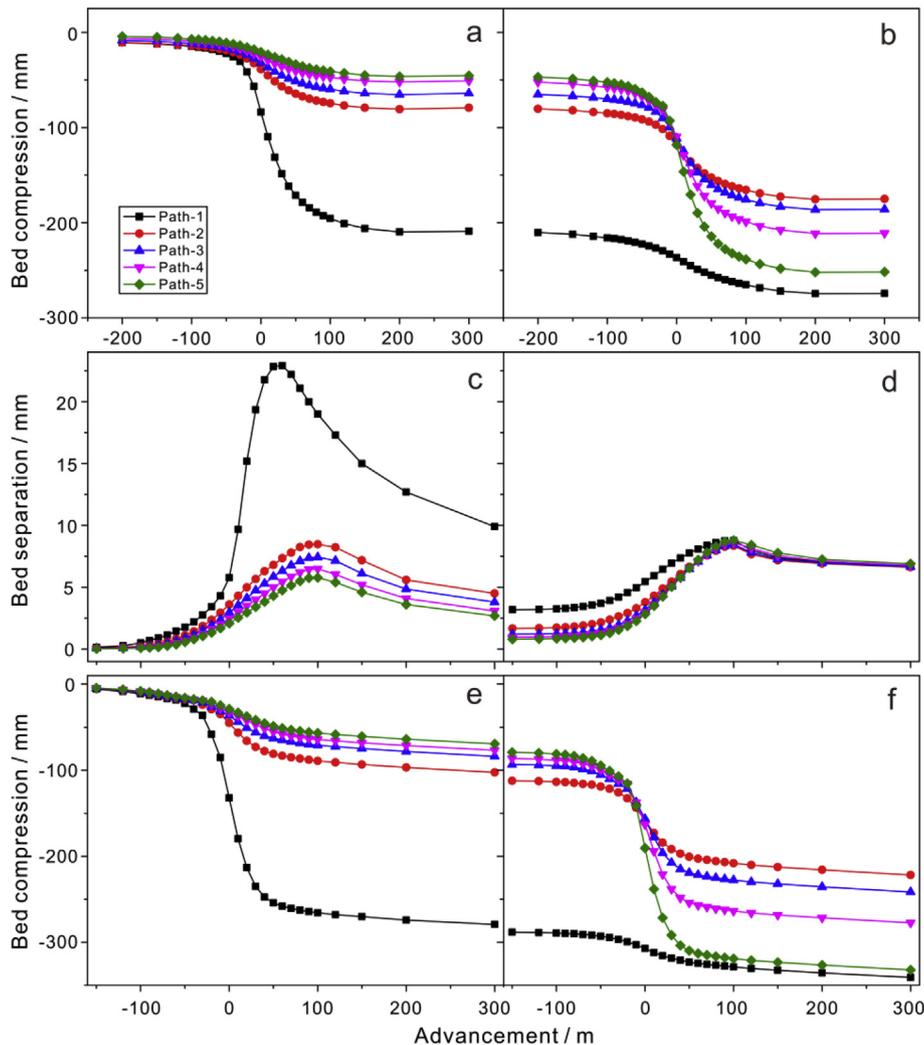

Fig. 12. Dynamic evolution of the largest bed separation ($\Delta d > 0$) and compression ($\Delta d < 0$) along well axes occurring at weak interfaces for the five candidate paths of wells piercing both shallow (100 m, a, b) and deep (300 m, c−f) seams. Δd are induced above and below a longwall pillar flanked by twin panels as they advance sequentially. Panel 1 is first extracted (a, c, e) followed by panel 2 (b, d, f).

path 5 (~40 mm) when mining panel 2, irrespective of mining depth.

4.1.3. Bed separation and compression − Δd

We record the vertical relative motion of two adjacent layers (Δd), in extension (separation) (Δd > 0) and in compression (Δd < 0) (Fig. 2 and Table 2) separately represent the tensile and compressive deformation occurring between alternating layers. Evolution of these bed separations and compressions as the twin panels sequentially advance are shown in Fig. 12 for mining at a depth of 100 m and 300 m. Since the largest bed separation for shallow mining (100 m) only accounts for 2 mm in the entire mining cycle, they are not displayed in Fig. 12.

As the working face moves progressively forward, the roof above the pillar edge begins to rotate and to sag, resulting in considerable compression between alternating hard and soft layers, especially between the seam and its immediate roof and floor. For shallow mining (100 m), the largest bed separation is ~2 mm for path 2 which occurs on an interface close to the surface (Table 2), where it is compressed and switches to compression as panel 1 advances. Bed separations for other wells are all less than 2 mm and ultimately switch to bed compressions. In the mining cycle of panel 2, the largest bed separation is 0.4 mm (path 1), which also occurs on the top interface. As for bed compression, they all increase gradually as the twin panels advance. The largest bed compressions at wells are separately ~209 mm and ~274 mm after single panel 1 and then both panels are extracted (Table 2). Bed compression is much larger for paths 1 and 5 which are closest to the flanking panels after both panels are mined, and path 2, which is closest to the pillar center, suffers the smallest bed compression. Along the longitudinal direction, bed compressions at interfaces between the seam and its immediate roof and floor are greatest (Fig. 13 and Table 2).

For deep mining (300 m), the greatest bed separation accounts for ~23 mm in the mining cycle of panel 1, which is for path 1 and occurs at an elevation 30 m above the seam when panel 1 advances 50 m beyond the well (Fig. 12 and Table 2). Bed separations of other wells do not exceed 10 mm. Bed separations increase as panel 2 approaches then passes these wells by ~100 m when they become invariant with a permanent set (~7 mm). Bed compressions increase progressively as the twin panels advance in succession. In the mining cycle of panel 1, the peak bed compression of path 1 (−279 mm) is much larger compared with that for paths 2−5 (<−102 mm). In the mining cycle of panel 2, inter-lamellar compressions increase continuously, and increase faster as panel 2 advances 10 m ahead of and 30 m beyond the wells. As panel 2 proceeds sufficiently far after these wells, paths 1 and 5 have the greatest cumulate inter-lamellar compressions, which are each ~340 mm, occurring in the vicinity of the seam (Fig. 13 and Table 2). Excessive bed separation and compression would induce tensile and compressive failure for wells along their axes requiring ductile or reinforced well casings to resist longitudinal compression.

4.2. Evolution of longitudinal well distortions, lateral and vertical strains

Beside bed slippage, separation and compression between alternating soft and stiff layers can result in shear, tensile and compressive failure. For wells subject to the influence of longwall mining, the high mining-induced strains at corners of the working face, where the front and the side abutment pressure superimpose (Fig. 7) are also destructive to the integrity of wells located within the pillar. Consequently, evolution and magnitudes of strains in mining cycles of the twin flanking panels are critical and need to be
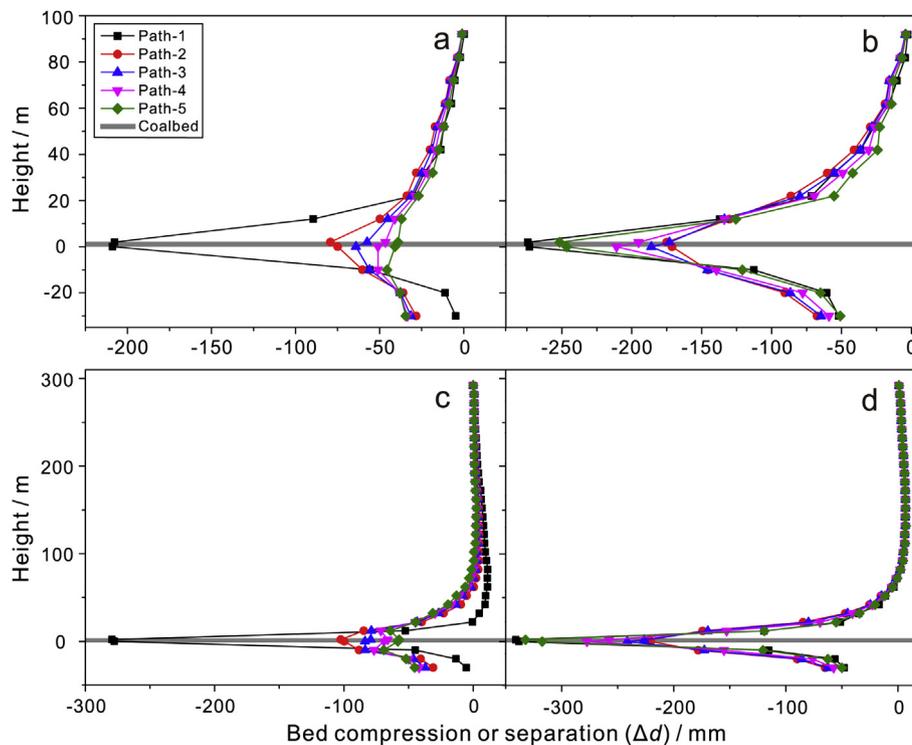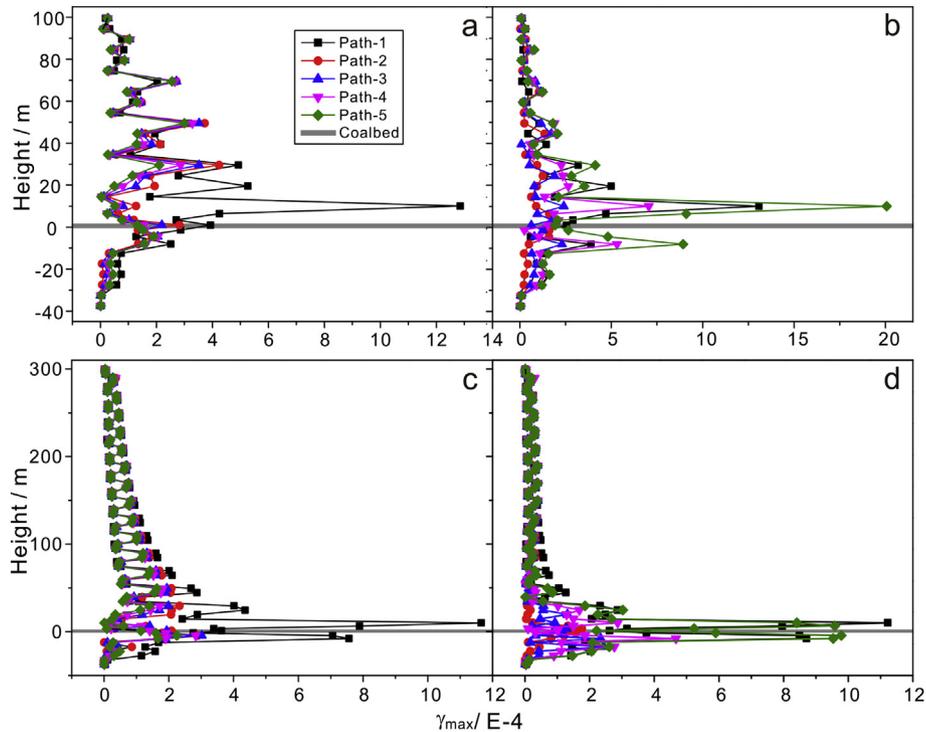

Fig. 13. Longitudinal distribution of bed separation (Δd > 0) and compression (Δd < 0) occurring at weak interfaces for the five candidate paths of wells after the single panel 1 (a, c) and then panel 2 (b, d) separately advance sufficiently far (300 m for wells piercing the 100 m deep seam (a, b) and 150 m for wells piercing the 300 m deep seam (c, d)) after these wells.
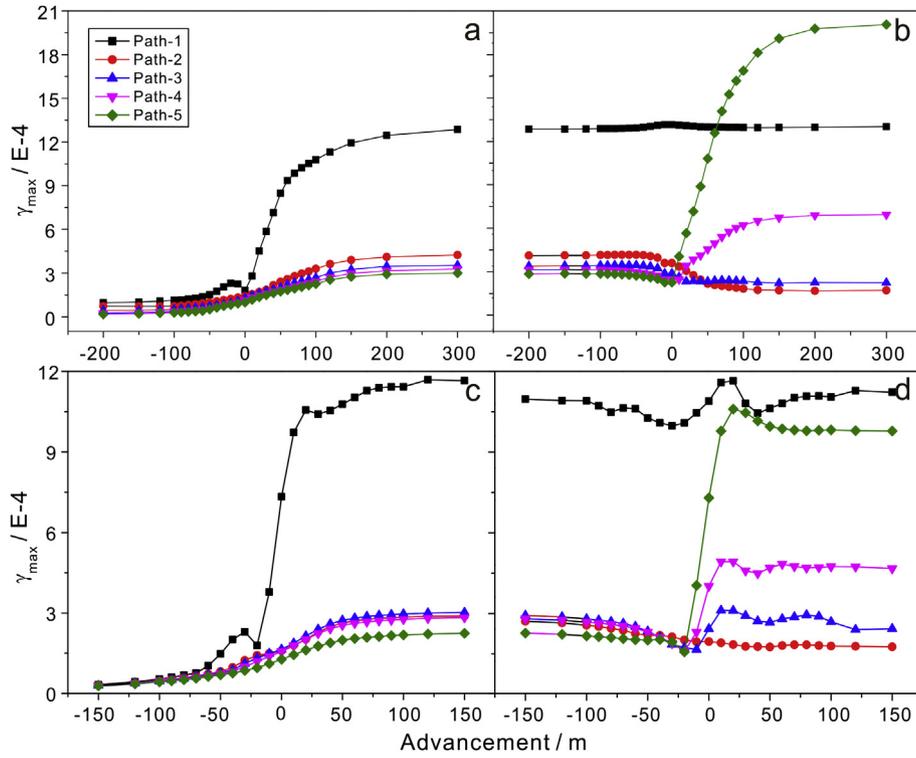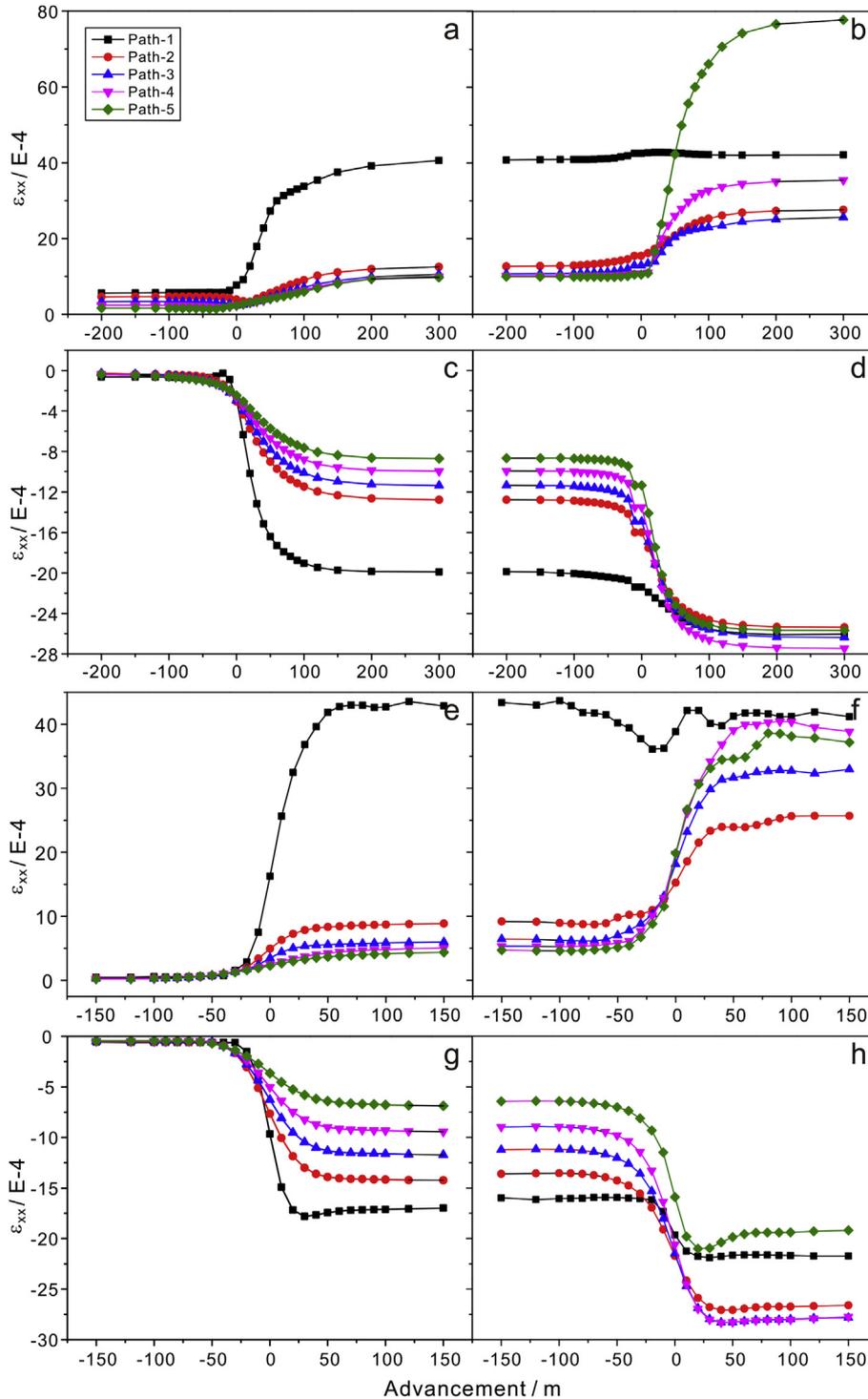
Fig. 14. Dynamic evolution of the largest total longitudinal well distortions (γ_{max}s) for the five candidate paths of wells piercing both the shallow (100 m) (a, b) and the deep (300 m) (c, d) seams as the twin flanking panels advance sequentially. Panel 1 is first extracted (a, c) followed by panel 2 (b, d).

investigated. We analyze the total longitudinal well distortion (γ_{max}) and its two components (γ_{xz}, γ_{yz}) that develop for wells piercing both the shallow (100 m) and the deep (300 m) seams. These distortions are equivalent to changes in lateral displacement with depth. We also analyze the horizontal strains (ε_{xx}, ε_{yy}) and vertical strain (ε_{zz}) along wells which might engender tensile and compressive failure in the casings. Model results are shown in Figs. 14–19 and Table 3.

Fig. 15. Distribution of the total longitudinal well distortions (γ_{max}s) for the five candidate paths of wells after the single panel 1 (a, c) and then panel 2 (b, d) separately advance sufficiently far (300 m for wells piercing the 100 m deep seam (a, b) and 150 m for wells piercing the 300 m deep seam (c, d)) after these wells.

Fig. 16. Dynamic evolution of the largest horizontal strains along well axes − ε_{xx}, the component along the direction parallel to the face (both the positive and negative) for the five candidate paths of wells piercing both the shallow (100 m, a–d) and the deep (300 m, e–h) seams as the twin flanking panels advance sequentially. Panel 1 is extracted first (a, c, e, g) and then panel 2 (b, d, f, h).

4.2.1. Total longitudinal well distortions − γ_{max}

Evolution of the largest total longitudinal well distortions (γ_{max}s) (Fig. 14) for the five wells bears an analogy to that of the largest total horizontal shear offsets ($U_{off\text{-}H}$s) (Fig. 8) during the entire mining cycle of the twin panels. That is, irrespective of seam depth, γ_{max}s of wells augment progressively when panel 1 approaches and passes these wells and increase relatively faster than when panel 1 advances tens of meters (deep mining) and about one hundred meters (shallow mining) beyond the wells. In the mining cycle of panel 2, the development of γ_{max}s also undergoes a cycling through minor to severe deformations and then returning to minor deformations.

When mining is shallow (100 m), the largest γ_{max} (1.3 milli-strain) is for path 1 and occurs in the shallow roof (8 m above the
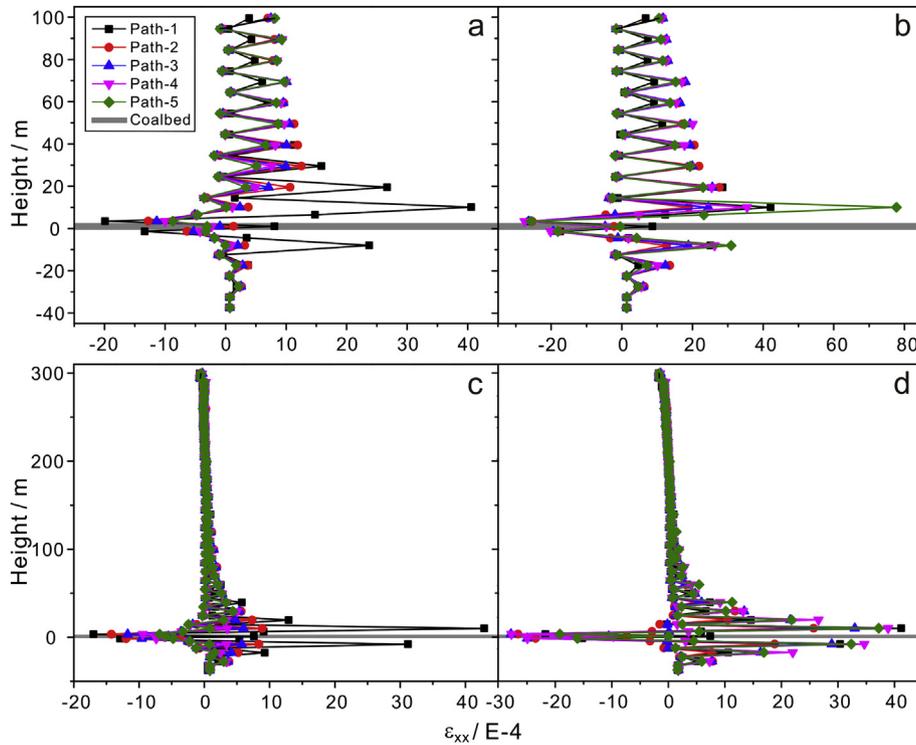
Fig. 17. Longitudinal distribution of horizontal strains (ε_{xx}) for the five candidate paths of wells after single panel 1 (a, c) and then panel 2 (b, d) separately proceed sufficiently far (300 m for wells piercing the 100 m deep seam (a, b) and 150 m for wells piercing the 300 m deep seam (c, d)) after these wells.

seam) as panel 1 advance ~200 m after wells. γ_{max}s of wells 2–5 are all less than 0.5 millistrain. In the mining cycle of panel 2, γ_{max} of path 1 remains almost constant; γ_{max}s of paths 2 and 3 decline slightly as panel 2 advances around the well and then becomes constant; but for paths 4 and 5, which are closer to panel 2, γ_{max}s switch from a slight decrease to a rapid increase as panel 2 passes alongside the wells. In the final steady-tending stage, the largest γ_{max} is maintained at ~2 millistrain, which is for path 5 and also evolves in the shallow roof. This is equivalent to ±20 mm horizontal displacement within one 10 m thick layer. When mining is deep (300 m), the largest γ_{max} of each path are all smaller to those in the case of shallow mining as either the single panel 1 or both panels are extracted. Irrespective of seam depth, paths 2 and 3 have smaller γ_{max}s after the twin panels are mined, both of which do not exceed 0.3 millistrain.

For shallow mining (100 m), the influence of mining on well distortion along the mining direction is more extensive. Longitudinal distortions (γ_{max}s) for wells closer to the twin panels begin to develop rapidly (increase or decrease) as panel 1 (path 1) and panel 2 (paths 5 and 4) pass alongside these wells, and asymptote after each panel advances more than one hundred meters beyond these wells. While for deep mining (300 m), the strong impact on well distortion is manifest earlier and lasts for a shorter distance. For instance, the largest γ_{max} along path 1 begins to increase sharply as panel 1 is ~20 m ahead of the well and tends to an ultimate steady magnitude as the panel advances ~20 m after the well. The largest γ_{max}s of paths 5 and 4 develop as panel 2 is ~20 m ahead of and ~10 m beyond the wells, respectively.

Regardless of mining depth, the largest γ_{max}s along the well axes all arise in the shallow roof (8 m above the seam), where the well is distressed by distortion. Also, wells closer to panels (paths 1 and 5) have the larger distortions as panel 1 and then panel 2 are sequentially extracted.

Evolution of the two components (γ_{xz} and γ_{yz}) of the total

longitudinal distortion (γ_{max}) is not presented here. The pattern and magnitude of evolution of γ_{xz} is similar to that of γ_{max} as the twin panels approach and then pass the wells. γ_{xz} contributes most to γ_{max}. For shallow mining, the component − γ_{xz}s, are respectively −0.3 to 1.3 millistrain and −2.0 to 1.3 millistrain after first panel 1 has passed and then after panel 2 is extracted; and for deep mining, they are −0.8 to 1.2 millistrain and −1.0 to 1.2 millistrain respectively (Table 3). The other component − γ_{yz}, is much smaller (<±0.4 millistrain). Evolution of γ_{yz} displays approximate symmetry as each panel advances, the symmetry plane lags behind the wells by 10 m for shallow mining and abreast of the wells for deep mining. γ_{yz}s increases first as the panel approaches the well and reaches a peak when the panel advances to the plane of symmetry thereafter γ_{yz}s decreases progressively.

4.2.2. Horizontal strains -ε_{xx} and ε_{yy}

Evolution and magnitudes of horizontal strains for wells penetrating both shallow and deep seams are shown in Figs. 16 and 17 and Table 3. Horizontal strain along the working face (ε_{xx}) is far larger than that along the mining direction (ε_{yy}), whose evolution is not presented in the figures. Evolution of ε_{xx}s also displays staged characteristics and bears an analogy to that of bed compression in the complete mining cycle of panels. Generally, irrespective of seam depth, ε_{xx}s increases as the twin panels are successively removed (Fig. 16). ε_{xx}s begin to increase rapidly as each advancing panel approaches within tens of meters and stabilizes to background as each panel passes the well by tens (deep mining) or up to more than one hundred (shallow mining) meters. ε_{xx}s are all principally extensional (positive) along most of the lengths of wells, and reach a peak in the shallow roof (+8 m) above the seam (Fig. 17). Horizontal compressive strains (negative) are restricted in the vicinity of the seam and are greatest at elevations immediately above and below the pillar (±1.5 m) (Fig. 17). The ranges of ε_{xx}s are respectively −2.0 to 4.1 millistrain and −2.8 to 7.8 millistrain after
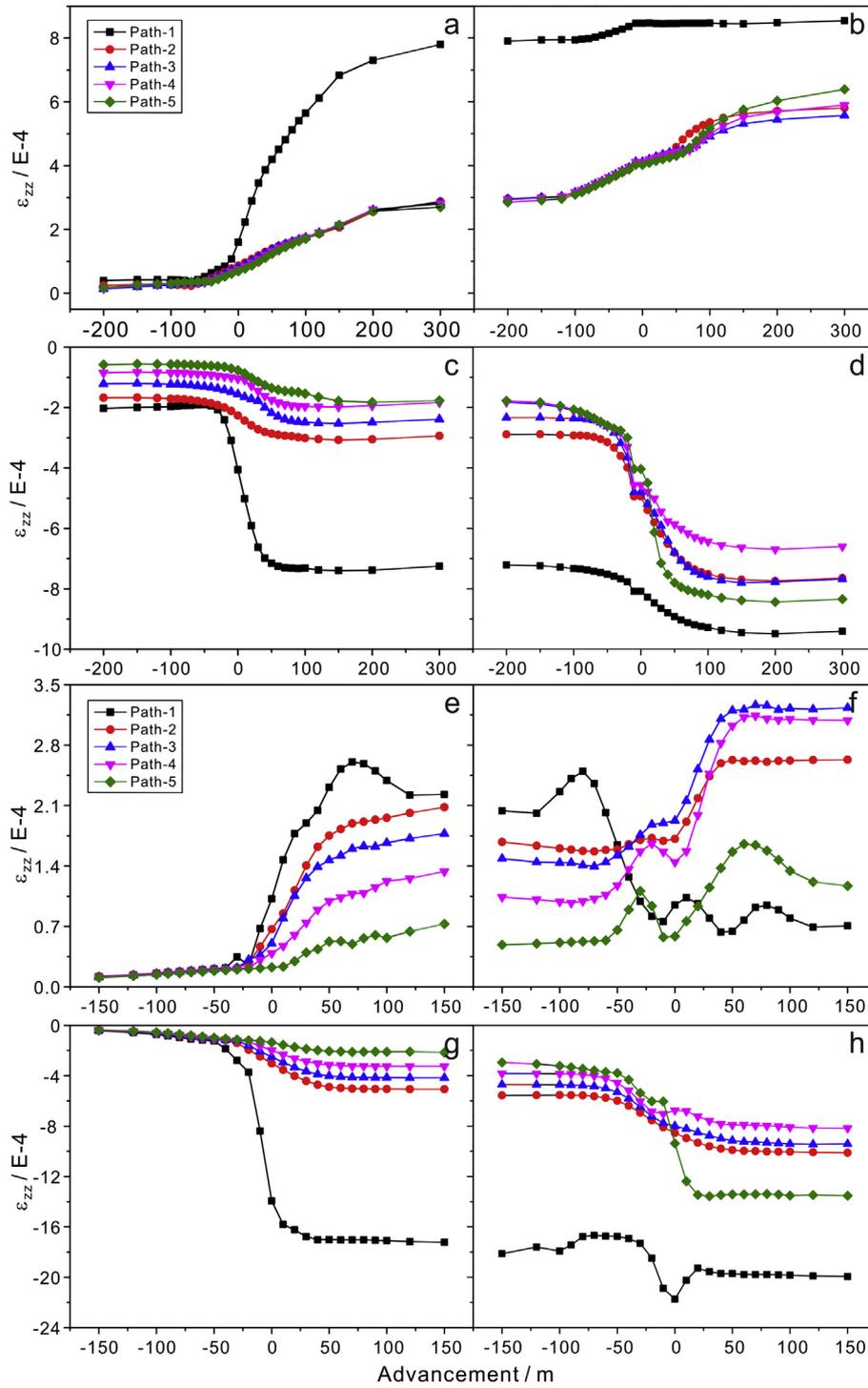
Fig. 18. Dynamic evolution of the largest vertical strains (ε_{zz}s) (both the positive and negative) along well axes for the five candidate paths of wells piercing both the shallow (100 m, a−d) and the deep (300 m, e−h) seams as the twin flanking panels advance sequentially. Panel 1 is extracted first (a, c, e, g) and then panel 2 (b, d, f, h).
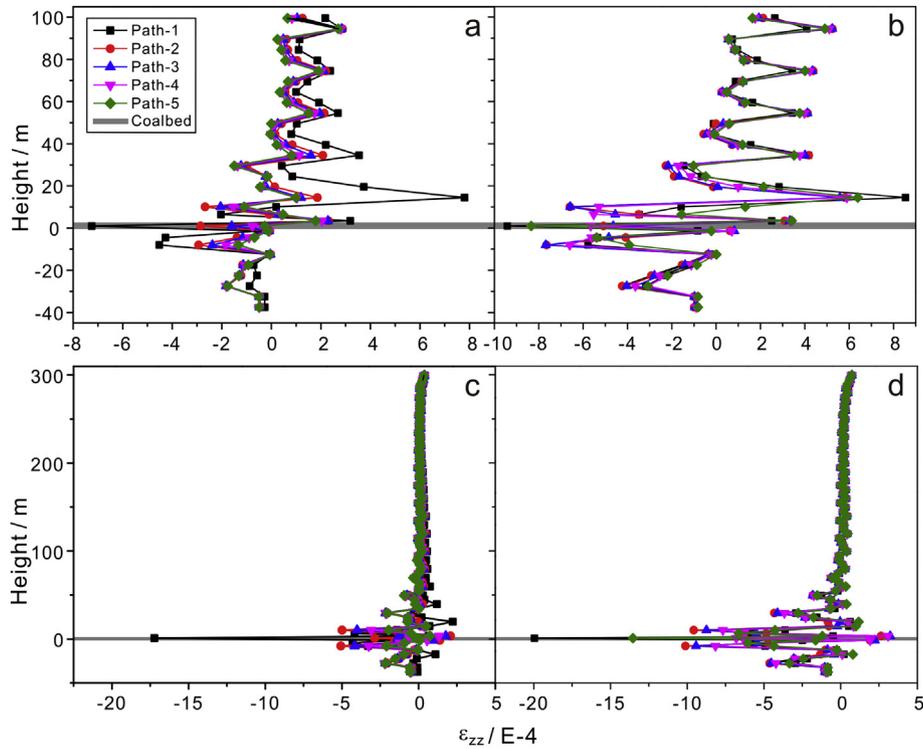
Fig. 19. Longitudinal distribution of vertical strains (ε_{zz}s) for the five candidate paths of wells after single panel 1 (a, c) and then panel 2 (b, d) separately proceed sufficiently far (300 m for wells piercing the 100 m deep seam (a, b) and 150 m for wells piercing the 300 m deep seam (c, d)) after these wells.

first panel 1 and then panel 2 are sequentially extracted for wells piercing the shallow seam (100 m). They change to be −1.8 to 4.4 millistrain and −2.8 to 4.4 millistrain respectively when mining is deep (300 m). Wells deform more severely by tension or compression in the horizontal plane in the vicinity of the seam (Fig. 17) especially as the second panel advances within tens (deep mining) and more than a hundred (shallow mining) meters beyond these wells (Fig. 16).

4.2.3. Vertical strains - ε_{zz}

As apparent in Fig. 18 there is a strong influence of the second advancing panel on the evolution of vertical strains (50−100 m ahead of wells) compared to those resulting from the first-mined panel (20−50 m ahead of wells). This is because plastic

deformations developed during the mining of panel 1 contribute additively to those developed during the mining of panel 2. The development of vertical strains both ahead of and after the passing of the face is broader when mining is shallow. Irrespective of mining depth, ε_{zz}s are principally extensional along most of the length of the wells (Fig. 19). Peak vertical extensile strains all arise in the shallow roof (at an elevation of 13 m and 1.5 m above the seam for the shallow and deep mining cases, respectively), and the peak vertical compressive strains all arise within the seam.

On the whole, regardless of seam depth, both the compressive and extensional vertical strains grow progressively as panels 1 and 2 advance sequentially, and grow faster as each panel proceeds around these wells. Ranges of vertical strains, in the case of shallow

Table 3
Statistical results of various strains and their components (longitudinal distortions, horizontal and vertical strains) for wells piercing a seam at a depth of 100 m and 300 m in the mining cycles of panels 1 and 2.

Seam depth	Strain/E-4	Panel 1	Hazardous locations/m		Panels 1 and 2	Hazardous locations/m		Percentage change
			Height	Advancement		Height	Advancement	
100 m	γ_{max}	13	8	>+120	20	8	>+120	54%
	γ_{xz}	−3 to 13	–	–	−20 to 13	–	–	–
	γ_{yz}	−1 to 2	–	–	−1 to 3	–	–	–
	ε_{xx}	−20 to 41	1.5/8	>+150	−28 to 78	1.5/8	>+150	40%−90%
	ε_{yy}	−3 to 4	–	+40	−3 to 5	–	+40	–
	ε_{zz}	−8 to 8	0/13	>+70	−10 to 9	0/13	>+120	25%−13%
300 m	γ_{max}	12	8	>+20	12	8	>+20	0
	γ_{xz}	−8 to 12	–	–	−10 to 12	–	–	–
	γ_{yz}	−2 to 3	–	–	−2 to 3	–	–	–
	ε_{xx}	−18 to 44	1.5/8	>+50	−28 to 44	1.5/8	>+50	56%−0
	ε_{yy}	−5 to 7	–	+20	−4 to 7	–	+20	–
	ε_{zz}	−17 to 3	0/1.5	>+50	−22 to 3	0/1.5	>+50	29%−0

Note: Hazardous height refers to an elevation (m) above the coal seam where various strains reach the peak and the well is most likely to fail; and the height "0" represents vertical compressive strains are largest within the seam.

mining, are −0.8 to 0.8 millistrain and −1 to 0.9 millistrain after first panel 1 and then panel 2 are extracted successively, and they change to −1.7 to 0.3 millistrain and −2.2 to 0.3 millistrain correspondingly when mining is deep (Table 3). Consequently, wells are more likely to crush by compression along their axes in the seam especially as the second panel advances tens (deep mining) and more than a hundred (shallow mining) meters beyond these wells (Figs. 18 and 19).

5. Conclusions

The redistribution and concentration of strains induced by the movement of overlying strata resulting from full extraction mining are a fundamental threat to the stability of gas wells piercing active longwall panels. We explore and define the anticipated distribution and magnitudes of deformations likely to potential wells and their dynamic evolution during the mining cycle by means of a stepwise excavation through a large scale three dimensional finite element model. This model represents a realistic representation of the evolving mining geometry and in situ conditions to return anticipated strains as they evolve around the multiple panel geometry. Through this study, the following conclusions are drawn:

(1) The effects of longwall mining on the stability of gas wells piercing a longwall pillar display staged characteristics as the twin flanking panels first approach then pass by these wells, first on one side (panel 1) and then the other (panel 2). Evolution of various well deformations may be cyclic and peak as the panel face passes closest to the well and then wane − only to repeat as the panel passes on the other side of the pillar. The severity of the maximum effects varies with seam depth and the relative distances between wells and ribs of the twin flanking panels. Wells begin to undergo accelerated or significant deformation (increase or decrease) when each advancing panel is tens of meters away and the deformation stabilizes as each panel passes the well by tens (deep mining, ~300 m) or more than a hundred (shallow mining, ~100 m) meters. Wells are more susceptible to instability after each panel, especially the second panel, advances approximately 50 m past the well in the case of deep mining and more than a hundred meters in that of shallow mining with the accumulative deformation reaching the maximum.

Both the total horizontal shear offsets (U_{off-H}s) and the total longitudinal distortions (γ_{max}s) of wells increase progressively during the advance of the first panel. However, it depends on different wells in the mining cycle of the second panel, U_{off-H}s and γ_{max}s for wells closer to the first advancing panel decrease gradually or remain constant, but for wells closer to the second mined panel, they evolve from slow decline to fleet increase. Respective components of U_{off-H}s and γ_{max}s associated with the direction parallel to the working face − U_{off-x}s and γ_{xz}s, also display similar evolutionary characteristics and magnitudes to those of them (U_{off-H}s and γ_{max}s). While for components associated with the advancing direction (U_{off-y}s and γ_{yz}s), they are far smaller and show approximate symmetry as each panel proceeds. As regards bed compression, horizontal and vertical strains, substantially, they all increase monotonously as each panel approaches and passes by these wells, and tend to be invariant as each panel advances tens (deep mining) and more than one hundred (shallow mining) meters beyond these wells.

(2) Along the longitudinal direction, wells are prone to shear on weak interfaces both in the shallow roof (irrespective of

seam depth) and close to the surface (only for shallow mining), especially on weak interfaces with a stiff layer above and a soft one below. Irrespective of mining depth, wells might fail by the combined impacts of distortion, tension and compression in the vicinity of the seam. Through a comprehensive evaluation of various well deformations in the whole mining cycle of longwall panels around the well, it is advisable to locate the well slightly closer to the rib of the second advancing panel, in which case, improved well integrity can be achieved.

(3) For mining at shallow depths (~100 m), rock movement and deformation within the thinner overlying strata of the seam are more severe, and the range of strong influence induced by shallow mining is relatively broad along both the transverse and mining directions. While for deep mining (~300 m), strata movement (and associated deformation of wells) is mainly restricted to the shallow roof, and engenders a smaller influence along the mining direction.

Acknowledgments

References

Aadnoy, B.S., Chenevert, M.E., 1987. Stability of highly inclined boreholes (includes associated papers 18596 and 18736). SPE Drill. Eng. 2, 364–374.

Aadnoy, B.S., Ong, S., 2003. Introduction to special issue on borehole stability. J. Petroleum Sci. Eng. 38 (3–4), 79–82.

Ajalloeian, R., Lashkaripour, G.R., 2000. Strength anisotropies in mudrocks. Bull. Eng. Geol. Env. 59, 195–199.

Al-Ajmi, A.M., Zimmerman, R.W., 2006. Stability analysis of vertical boreholes using the Mogi–Coulomb failure criterion. Int. J. Rock Mech. Min. Sci. 43 (8), 1200–1211.

Bradley, W.B., 1979a. Mathematical concept − stress cloud − can predict borehole failure. Oil Gas. J. (United States) 77 (8). Medium: X; Size: Pages: 92-96, 101–102.

Bradley, W.B., 1979b. Failure of inclined boreholes. J. Energy Resour. Technol. 101, 232–239.

Chen, J., Wang, T., Zhou, Y., Zhu, Y., Wang, X., 2012. Failure modes of the surface venthole casing during longwall coal extraction: a case study. Int. J. Coal Geol. 90–91, 135–148.

Elsworth, D., Liu, J., 1995. Topographic influence of longwall mining on groundwater supplies. Ground Water 33, 786–793.

Gough, D.I., Bell, J.S., 1981. Stress orientations from oil-well fractures in Alberta and Texas. Can. J. Earth Sci. 18, 638–645.

Gutierrez, J.J., Vallejo, L.E., Lin, J.S., 2010. A Study of Highway Subsidence Due to Longwall Mining Using Data Collected from I-79. Pennsylvania Department of Transportation (Contract #510601).

Haimson, B.C., Song, I., 1993. Laboratory study of borehole breakouts in Cordova Cream: a case of shear failure mechanism. Int. J. Rock Mech. Min. 30, 1047–1056.

Hale, A., Mody, F., 1993. Borehole-stability model to couple the mechanics and chemistry of drilling-fluid/shale interactions. J. Petroleum Technol. 45 (11), 1093–1101.

Hale, A.H., Mody, F.K., Salisbury, D.P., 1993. The influence of chemical potential on wellbore stability. SPE Drill. Complet. 8 (3), 207–216.

Haluszczak, L.O., Rose, A.W., Kump, L.R., 2013. Geochemical evaluation of flowback brine from Marcellus gas wells in Pennsylvania, USA. Appl. Geochem. 28 (0), 55–61.

Itasca, 2009. FLAC3D Version 4. 0. Itasca Consulting Group Inc, Minneapolis, Minnesota.

Karacan, C.Ö., 2009a. Forecasting gob gas venthole production performances using intelligent computing methods for optimum methane control in longwall coal mines. Int. J. Coal Geol. 79, 131–144.

Karacan, C.Ö., 2009b. Reconciling longwall gob gas reservoirs and venthole production performances using multiple rate drawdown well test analysis. Int. J. Coal Geol. 80, 181–195.

Karacan, C.Ö., Goodman, G., 2009. Hydraulic conductivity changes and influencing

factors in longwall overburden determined by slug tests in gob gas ventholes. Int. J. Rock Mech. Min. Sci. 46, 1162—1174.

Karacan, C.Ö., Olea, R.A., 2013. Sequential Gaussian co-simulation of rate decline parameters of longwall gob gas ventholes. Int. J. Rock Mech. Min. Sci. 59, 1—14.

Lee, H., Ong, S.H., Azeemuddin, M., Goodman, H., 2012. A wellbore stability model for formations with anisotropic rock strengths. J. Pet. Sci. Eng. 96—97, 109—119.

Liang, S., Elsworth, D., Li, X., Yang, D., 2014. Topographic influence on stability for gas wells penetrating longwall mining areas. Int. J. Coal Geol. 132, 23—36.

Liu, J., Elsworth, D., 1997. Three-dimensional effects of hydraulic conductivity enhancement and desaturation around mined panels. Int. J. Rock Mech. Min. Sci. 34, 1139—1152.

Liu, J., Elsworth, D., 1999. Evaluation of pore water pressure fluctuation around an advancing longwall face. Adv. Water Resour. 22, 633—644.

Liu, C., Zhou, F., Yang, K., Xiao, X., Liu, Y., 2014. Failure analysis of borehole liners in soft coal seam for gas drainage. Eng. Fail. Anal. 42 (0), 274—283.

Luo, J., 1997. Gateroad Design in Overlying Multi-seam Mines. Mastersthesis. Virginia Polytechnic Institute and State University.

McNally, G., Evans, R., 2007. Impacts of Longwall Mining on Surface Water and Groundwater, Southern Coalfield NSW. Prepared by EWater CRC for NSW Department of Environment and Climate Change. eWater Cooperative Research Centre, Canberra.

Mohammad, N., Lloyd, P.W., Reddish, D.J., 1997. Longwall surface subsidence prediction through numerical modelling. In: Proc. of 16th Inter. Conf. on Ground Control in Mining, Morgantown, West Virginia, pp. 33—42.

Niandou, H., Shao, J.F., Henry, J.P., Fourmaintraux, D., 1997. Laboratory investigation of the mechanical behaviour of tournemire shale (vol 34, pg 3, 1997). Int. J. Rock Mech. Min. Sci. 34, 3—16.

Ong, S.H., Roegiers, J.C., 1993. Influence of anisotropies in borehole stability. Int. J. Rock Mech. Min. 30, 1069—1075.

Peng, S.S., 1986. Coal Mine Ground Control, second ed. Wiley, New York.

Peng, S.S., 1992. Surface Subsidence Engineering. Society for Mining, Metallurgy, and Exploration, Inc, Littleton, Colorado.

Peng, S.S., Chiang, H.S., 1984. Longwall Mining. John Wiley & Sons, New York.

Rostami, J., Elsworth, D., Watson, R., 2012. Study of Borehole Stability for Gas Wells in Longwall Mining Areas (Report Submitted to Range Resources).

Santarelli, F.J., Brown, E.T., Maury, V., 1986. Analysis of borehole stresses using pressure dependent, linear elasticity. Int. J. Rock Mech. Min. 23, 445—449.

Schatzel, S.J., Karacan, C.Ö., Dougherty, H., Goodman, G.V.R., 2012. An analysis of reservoir conditions and responses in longwall panel overburden during mining and its effect on gob gas well performance. Eng. Geol. 127 (0), 65—74.

Scovazzo, V.A., Russell, P.M., 2013. Industry research into gas and oil well protective coal pillar design. In: 32nd International Conference on Ground Control in Mining, Morgantown, WV, pp. 45—52.

Shabanimashcool, M., Li, C.C., 2012. Numerical modelling of longwall mining and stability analysis of the gates in a coal mine. Int. J. Rock Mech. Min. Sci. 51 (0), 24—34.

Singh, M.M., Kendorski, F.S., 1981. Strata disturbance prediction for mining beneath surface water and waste impoundments. In: Proc. 1st Conference on Ground Control in Mining, Morgantown, WV.

Tan, C.P., Willoughby, D.R., 1993. Critical mud weight and risk contour plots for designing inclined wells. In: The 68th Annual Technical Conference and Exhibition of the Society of Petroleum Engineers, Houston, Texas, pp. 101—115.

Tan, C., Richards, B., Rahman, S.S., 1996. Managing physico-chemical wellbore instability in shales with the chemical potential mechanism. In: Asia Pacific Oil and Gas Conference, Adelaide, pp. 107—116.

Tan, C.P., Rahman, S.S., Richards, B.G., Mody, F.K., 1998. Integrated Rock Mechanics and Drilling Fluid Design Approach to Manage Shale Instability (SPE/ISRM Rock Mechanics in Petroleum Engineering).

Tien, Y.M., Kuo, M.C., Juang, C.H., 2006. An experimental investigation of the failure mechanism of simulated transversely isotropic rocks. Int. J. Rock Mech. Min. Sci. 43, 1163—1181.

Wang, Y., Watson, R., Rostami, J., Wang, J., Limbruner, M., He, Z., 2013. Study of borehole stability of Marcellus shale wells in longwall mining areas. J. Petrol. Explor. Prod. Technol. 1—13.

Whittles, D.N., Lowndes, I.S., Kingman, S.W., Yates, C., Jobling, S., 2006. Influence of geotechnical factors on gas flow experienced in a UK longwall coal mine panel. Int. J. Rock Mech. Min. Sci. 43 (3), 369—387.

Whittles, D.N., Lowndes, I.S., Kingman, S.W., Yates, C., Jobling, S., 2007. The stability of methane capture boreholes around a long wall coal panel. Int. J. Coal Geol. 71, 313—328.

Wu, H.M., Shu, Y.M., Zhu, J.G., 2011. Implementation and verification of interface constitutive model in FLAC3D. Water Sci. Eng. 4 (3), 305—316.

Yavuz, H., Fowell, R.J., 2002. Softening effect of coal on the design of yield pillars. In: Proc of the 2nd Inter. FLAC Conf. Lyon, France, pp. 313—320.

Zeynali, M.E., 2012. Mechanical and physico-chemical aspects of wellbore stability during drilling operations. J. Pet. Sci. Eng. 82—83, 120—124.

Zhang, X., Last, N., Powrie, W., Harkness, R., 1999. Numerical modelling of wellbore behaviour in fractured rock masses. J. Petroleum Sci. Eng. 23 (2), 95—115.

Zhang, J., Lang, J., Standifird, W., 2009. Stress, porosity, and failure-dependent compressional and shear velocity ratio and its application to wellbore stability. J. Petroleum Sci. Eng. 69 (3—4), 193—202.